

Spectral Function Space Learning and Numerical Linear Algebra Networks for Solving Linear Inverse Problems

Andrea Aspri⁴

andrea.aspri@unimi.it

Leon Frischauf¹

leon.frischauf@univie.ac.at

Otmar Scherzer^{1,2,3}

otmar.scherzer@univie.ac.at

¹Faculty of Mathematics
University of Vienna
Oskar-Morgenstern-Platz 1
A-1090 Vienna, Austria

²Johann Radon Institute for Computational
and Applied Mathematics (RICAM)
Altenbergerstraße 69
A-4040 Linz, Austria

³Christian Doppler Laboratory
for Mathematical Modeling and Simulation
of Next Generations of Ultrasound Devices
(MaMSi)
Oskar-Morgenstern-Platz 1
A-1090 Vienna, Austria

⁴Università degli Studi di Milano Statale
Department of Mathematics
“Federigo Enriques”
Via Saldini, 50
20133 Milano, Italy

Abstract

We consider solving a probably ill-conditioned linear operator equation, where the operator is not modeled by physical laws but is specified via training pairs (consisting of images and data) of the input-output relation of the operator. We derive a stable method for computing the operator, which consists of first a Gram-Schmidt orthonormalization of images and a principal component analysis of the data. This two-step algorithm provides a spectral decomposition of the linear operator. Moreover, we show that both Gram-Schmidt and principal component analysis can be written as a deep neural network, which relates this procedure to de- and encoder networks. Therefore, we call the two-step algorithm a linear algebra network. Finally, we provide numerical simulations showing the strategy is feasible for reconstructing spectral functions and for solving operator equations without explicitly exploiting the physical model.

1. INTRODUCTION

We consider solving a probably ill-conditioned **linear operator equation**

$$F\mathbf{x} = \mathbf{y}, \quad (1.1)$$

where $\mathbf{x} \in \mathbb{R}^m$ and $\mathbf{y} \in \mathbb{R}^m$. We call \mathbb{R}^m the **image** and \mathbb{R}^m the **data space** following the terminology of [4, 3]. The main assumption of this work is that the operator F is **not** modeled by physical laws but indirectly via **training pairs**, $\mathcal{P} := \{(\mathbf{x}_i, \mathbf{y}_i) : i = 1, \dots, N\}$, which satisfy

$$F\mathbf{x}_i = \mathbf{y}_i \quad i = 1, \dots, N. \quad (1.2)$$

N is called the sampling size, and we denote the span of the training images and data by

$$X_N := \text{span}\{\mathbf{x}_i : i = 1, \dots, N\} \subseteq \mathbb{R}^m, \quad Y_N := \text{span}\{\mathbf{y}_i : i = 1, \dots, N\} \subseteq \mathbb{R}^m.$$

Without further notice, we always assume that the training images \mathbf{x}_i are linearly independent and that F has trivial nullspace, such that the training data \mathbf{y}_i are also linearly independent.

In this paper we study **learning** the operator F and its inverse by **en-** and **decoding**, which refer to exclusive use of training data. After learning the operator F , we can solve Equation 1.1 for arbitrary data $\mathbf{y} \in \mathbb{R}^m$. Operator learning is a very active field of research: There exist a variety of such methods, such as **black box** strategies (see, for instance, [25]) for linear operator learning. For nonlinear operators **deep neural network** learning can be used [17, 19, 18, 20]. For applications in inverse problems, see [1, 16].

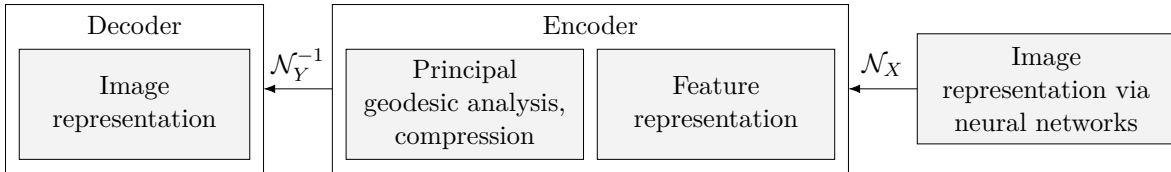


FIGURE 1. Variational en- and decoding with neural networks: The image data are represented via a neural network. After that they are transformed into a **feature** space (with the operator \mathcal{N}_X). The features are compressed by a principal geodesic analysis. The decoder \mathcal{N}_Y^{-1} (we assume for the sake of simplicity that the operator is invertible) transforms features into images.

Coding is a term used in **manifold learning**, which, in turn, is a basic tool in machine learning. The basic assumption there is that all potentially measured \mathbf{y} 's are elements of a **low-dimensional** manifold (see, for instance, [10, 7]). The setting of manifold learning (no operator connecting data) is represented in Figure 1. Our strategy for operator learning is conceptually similar to manifold learning but differs by the used techniques (compare Figure 1 and Figure 2). In this paper, we investigate coding for solving

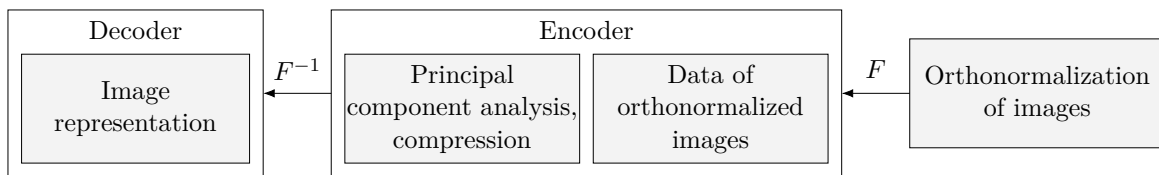


FIGURE 2. En- and decoding scheme for **linear** operators: First the image data are orthonormalized and the according data is computed by applying F - this is done by explicit calculations without making use on any physical model describing the forward operator. On the orthonormalized data a principal component analysis (PCA) is applied, which allows to compress the data space. The decoder calculates the inverse of some given data in the compressed space.

linear ill-posed problems as outlined in Figure 2. We show that orthonormalization is a key tool for operator learning (this is of course not a new observation, see for instance [11]). The paper is based on the following two truly interesting observations:

- (i) Figure 2 determines the singular vectors of F (see Theorem 2.6). In other words, the choice of the training pairs only influences which spectral vectors and values are determined. Related to this result are regularization issues: In [4, 3], we showed that orthonormalization of training data or training images (in a separate manner) can be used to stably determine an operator if the orthonormalization produces a basis that is close to the singular vectors. There is an anti-symmetry in the two approaches, which is overcome in this paper. In this context, regularization and stability analysis should not be confused. For instance, as used here, Gram-Schmidt orthonormalization is unstable with an increased number of expert pairs. However, regularization results apply if the pre-processing orthonormalization methods (like Gram-Schmidt) have been implemented in a stable manner. In other words, the truncated singular value decompositions (SVD) is a stable regularization method (presuming that the singular functions have been calculated exactly).
- (ii) Moreover, we show that each building block of Figure 2 (in particular orthonormalization) can be expressed via a customized **linear algebra network** (see Figure 3 in Section 2.1). The term customized refers that the parameters in the neural network are given by the algorithm and do not need to be optimized.
- (iii) Finally, we present some numerical experiments on learning the Radon operator (source code [2]). For this operator, the singular values are explicitly known (see [9, 22]). Therefore, we can compare the computed singular values from training data with the analytical ones. See Section 4. Although it is theoretically possible to recover singular vectors, practical handicaps are due to instabilities of the orthonormalization algorithms.

2. ENCODING OF LINEAR OPERATORS

The encoder from Figure 2 consists of two steps:

- (i) Calculating orthonormalized images.

(ii) Computing a principal component of data of orthonormalized images ($\bar{\mathbf{y}}_j := F(\bar{\mathbf{x}}_j), j = 1, \dots, N$).

We recall that according to our general assumptions, training images and data, respectively, and thus $N \leq \{\underline{m}, \bar{m}\}$. This will be assumed in the course of this paper.

2.1. Pre-processing - orthonormalization. We review the Gram-Schmidt orthonormalization method (see for instance [15]) and show that it can be expressed as a deep neural network (NN). In a second step we show that also QR decomposition, realizing PCA, is representable as a deep NN. In other words, they are **customized** because the parameters do not need to be optimized. Therefore, we call such networks **linear algebra networks**.

Gram-Schmidt as a deep network

We start with the training images $\mathbf{x}_1, \dots, \mathbf{x}_N \in \mathbb{R}^m$ and orthonormalize them iteratively. Let

$$\begin{aligned} \sigma : \mathbb{R}^m \setminus \{0\} &\rightarrow \mathbb{R}^m \\ \mathbf{x} &\mapsto \frac{\mathbf{x}}{\|\mathbf{x}\|} \end{aligned}$$

Then Gram-Schmidt looks as follows:

$$\bar{\mathbf{x}}_j := \sigma \left(\underbrace{\mathbf{x}_j - \sum_{i=1}^{j-1} \langle \mathbf{x}_j, \bar{\mathbf{x}}_i \rangle \bar{\mathbf{x}}_i}_{=: \rho(\mathbf{x}_j)} \right) \text{ for all } j = 1, \dots, N. \quad (2.1)$$

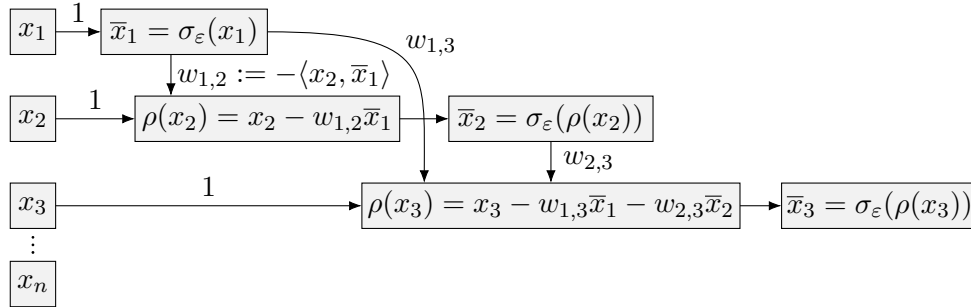


FIGURE 3. The neural network structure of the Gram-Schmidt orthonormalization. We use here the function σ_ε from Equation 2.2 as activation function.

Remark 2.1 In machine learning context instead of the high-dimensional signum function σ the smooth approximation

$$\begin{aligned} \sigma_\varepsilon : \mathbb{R}^m &\rightarrow \mathbb{R}^m \\ \mathbf{x} &\mapsto \frac{\mathbf{x}}{\sqrt{\|\mathbf{x}\|^2 + \varepsilon^2}} \end{aligned} \quad (2.2)$$

is used and called **activation function**. Replacing in Figure 3 σ by σ_ε we obtain an N -layer neural network, which we call **Gram-Schmidt network**. We note, however, that this is not a standard neural network (see, for instance, [6]) because there $\hat{\sigma}_\varepsilon : \mathbb{R}^1 \rightarrow \mathbb{R}^1$ is evaluated for each component of \mathbb{R}^N . Such network cannot be used here because we must ensure that every $\rho(\mathbf{x}_j), j = 1, \dots, N$ is a linear combination of $\mathbf{x}_i, i = 1, \dots, j - 1$. There are efficient alternatives to Gram-Schmidt, which are, for instance, block based (see, for instance, [8]), which can be reinterpreted again as deep neural networks. Gram-Schmidt breaks down if and only if one of the vectors $\rho(\mathbf{x}_j)$ becomes zero, or in other words, if the vectors $\mathbf{x}_j, j = 1, \dots, N$ become linearly dependent. We excluded this by a general assumption that all images are linearly independent. With a smooth approximation σ_ε , the linear dependence of the training images does not result in a break down of the algorithm described in Figure 3. In fact, all available training pairs can be used. However, the linear dependence assumption cannot be avoided for the analysis.

2.2. Data from orthonormalized images. If the nullspace of F is trivial, then from Equation 2.1 it follows immediately that (see Figure 3) that

$$\bar{\mathbf{y}}_j := F\bar{\mathbf{x}}_j := F(\sigma(\rho(\mathbf{x}_j))) = \frac{1}{\|\rho(\mathbf{x}_j)\|} F(\rho(\mathbf{x}_j)) \text{ for all } j = 1, \dots, N. \quad (2.3)$$

This means that the data of orthonormalized images can be computed without explicit knowledge of F . Note that $\rho(\mathbf{x}_j)$ is a linear combination of \mathbf{x}_i , $i = 1, \dots, j$.

With the knowledge of $\bar{\mathbf{y}}_j$, $j = 1, \dots, N$, we can compute data for every image $\mathbf{x} \in X_N$. Since

$$\mathbf{x} = \sum_{i=1}^N \langle \mathbf{x}, \bar{\mathbf{x}}_i \rangle \bar{\mathbf{x}}_i,$$

it follows that

$$\mathbf{y} = F\mathbf{x} = \sum_{i=1}^N \langle \mathbf{x}, \bar{\mathbf{x}}_i \rangle F\bar{\mathbf{x}}_i = \sum_{i=1}^N \langle \mathbf{x}, \bar{\mathbf{x}}_i \rangle \bar{\mathbf{y}}_i.$$

Remark 2.2 If instead of an exact Gram-Schmidt the deep network Gram-Schmidt from Figure 3 is used, we can apply the approximate formula with σ_ε from Equation 2.2 is used

$$\bar{\mathbf{y}}_j := F\bar{\mathbf{x}}_j \approx F(\sigma_\varepsilon(\rho(\mathbf{x}_j))) =: \frac{1}{\|\sigma_\varepsilon(\rho(\mathbf{x}_j))\|} F(\rho(\mathbf{x}_j)) \text{ for all } j = 1, \dots, N. \quad (2.4)$$

Principal component analysis (PCA). In the following, we analyze under which assumptions the PCA is stable. Starting point of this discussion is **Seidman's veto** [26], which states that regularization by projection is in general not a regularization method. This means that by projecting onto X_S inversion of F on the range of F of X_S is not stable. On the other hand if F is inverted on Y_S , then it is in fact stable (see again [26]). However, in the context of machine learning this requires to collect training data of $F^*\mathbf{y}_i$, $i = 1, \dots, S$, which is in general not available. As a conclusion from [26] we find that F can be stably inverted by projection if X_S is the space of the singular vectors corresponding to the largest S singular values (see for instance [12]). We emphasize again, that here stability refers to inversion of the truncated SVD after orthonormalization. Now, we show how this singular values can be calculated with machine learning techniques:

Theorem 2.3 (Spectral theory: See Theorem 2.5.2 in [15]) *Let the operator $F : \mathbb{R}^m \rightarrow \mathbb{R}^{\bar{m}}$ be linear. Then for every $\mathbf{x} \in \mathbb{R}^m$*

$$F\mathbf{x} = \sum_{j=1}^{\min\{m, \bar{m}\}} \gamma^j \langle \mathbf{x}, \mathbf{u}^j \rangle \mathbf{v}^j \text{ and } F^T \mathbf{v}^j = \gamma^j \mathbf{u}^j, F\mathbf{u}^j = \gamma^j \mathbf{v}^j, \quad (2.5)$$

where $\mathbf{u}^j \in \mathbb{R}^m$, $j = 1, \dots, \underline{m}$ and $\mathbf{v}^j \in \mathbb{R}^{\bar{m}}$, $j = 1, \dots, \bar{m}$ are orthonormal, respectively, and

$$0 \leq \gamma^1 \leq \gamma^2 \leq \dots \leq \gamma^{\min\{m, \bar{m}\}}.$$

In matrix form, this identity becomes more compact:

$$F = \mathbf{V}\mathbf{D}\mathbf{U}^T \text{ with } \mathbf{U} \in \mathbb{R}^{m \times m}, \mathbf{V} \in \mathbb{R}^{\bar{m} \times \bar{m}}, \quad (2.6)$$

where \mathbf{U} and \mathbf{V} are orthonormal and

$$\mathbf{D} = \text{diag}(\gamma^1, \gamma^2, \dots, \gamma^{\min\{m, \bar{m}\}}) \in \mathbb{R}^{\bar{m} \times m}.$$

In the following, we group the spectral values:

Definition 2.4 Let F be linear with trivial nullspace with spectral decomposition as in Equation 2.5. We denote by

$$\Gamma := \{\gamma^j : j = 1, \dots, \min\{\underline{m}, \bar{m}\}\} = \{\hat{\gamma}^k : k = 1, \dots, \hat{m}\} \quad (2.7)$$

the set of distinct singular values. Because F is assumed to have trivial nullspace $\gamma^j > 0$ for all $j = 1, \dots, \min\{\underline{m}, \bar{m}\}$. Moreover, we associate to each multiple singular value the associated singular vectors: For every $k = \{1, \dots, \hat{m}\}$ let

$$E^k := \text{span} \{\mathbf{v}^j : \gamma^j = \hat{\gamma}^k, j = 1, \dots, \min\{\underline{m}, \bar{m}\}\}. \quad (2.8)$$

Now, we apply the spectral theory to show that the proposed decoding algorithm is stable. There, we make some general notation:

Definition 2.5 Let $\bar{\mathbf{x}}_i, i = 1, \dots, N$ be the orthonormalized training images and $\bar{\mathbf{y}}_i, i = 1, \dots, N$ the according images as defined in Equation 2.1 and Equation 2.3, respectively. We denote:

$$\bar{\mathbf{X}} := (\bar{\mathbf{x}}_1, \dots, \bar{\mathbf{x}}_N) \in \mathbb{R}^{m \times N}, \quad \bar{\mathbf{Y}} = (\bar{\mathbf{y}}_1, \dots, \bar{\mathbf{y}}_N) \in \mathbb{R}^{\bar{m} \times N} \text{ and } A := \bar{\mathbf{Y}}\bar{\mathbf{Y}}^T \in \mathbb{R}^{\bar{m} \times \bar{m}}. \quad (2.9)$$

Note that by our general assumptions, the rank of each of the three matrices is always $N \leq \bar{m}$.

With this result, we can state the main result of this paper:

Theorem 2.6 Let $\psi_j \in \mathbb{R}^{\bar{m}}, j = 1, \dots, N$ be a non-zero eigenvector of A , then

- (i) there exists $k \in \{1, \dots, \hat{m}\}$ such that $\psi_j \in E^k$.
- (ii) This, in particular, means that if a non-zero eigenvector of A has multiplicity one, then it equals a spectral vector of F .

Proof: The PCA in image space calculates the eigenvalue decomposition of the covariance matrix

$$A := \bar{\mathbf{Y}}\bar{\mathbf{Y}}^T = \underbrace{\bar{\mathbf{W}} \begin{bmatrix} \Lambda \in \mathbb{R}^{N \times N} & 0 \\ 0 & 0 \end{bmatrix} \bar{\mathbf{W}}^T}_{=: \bar{\Lambda}} \in \mathbb{R}^{\bar{m} \times \bar{m}},$$

where $\bar{\mathbf{W}} \in \mathbb{R}^{\bar{m} \times \bar{m}}$ is an orthonormal matrix $\bar{\mathbf{W}}$ describes the principal directions of the data $\bar{\mathbf{Y}}$, and the according entries of D describe the elongation of the data in this direction. Now, since $\bar{\mathbf{Y}} = F\bar{\mathbf{X}}$, we get

$$F\bar{\mathbf{X}}\bar{\mathbf{X}}^T F^T = \bar{\mathbf{Y}}\bar{\mathbf{Y}}^T = \bar{\mathbf{W}}D\bar{\mathbf{W}}^T. \quad (2.10)$$

Since $\bar{\mathbf{X}}$ consists of orthonormal vectors and has rank N we have

$$\bar{\mathbf{X}}\bar{\mathbf{X}}^T = \begin{bmatrix} \mathcal{I} \in \mathbb{R}^{N \times N} & 0 \\ 0 & 0 \end{bmatrix} =: \bar{\mathcal{I}} \in \mathbb{R}^{m \times m},$$

where \mathcal{I} is the unitary matrix. Let $\mathbf{U} \in \mathbb{R}^{m \times m}$ be orthonormal as in Equation 2.6, then, after reordering of columns of $\bar{\mathbf{X}}$,

$$\mathbf{U}^T \bar{\mathbf{X}}^T \bar{\mathbf{X}} \mathbf{U} = \mathbf{U}^T \bar{\mathcal{I}} \mathbf{U} \in \mathbb{R}^{m \times m}.$$

The matrix $\bar{\mathcal{I}}\mathbf{U}$ projects onto the first basis vectors \mathbf{u}_i (after reordering). Then we get from Equation 2.10 and Equation 2.6 the identity

$$\bar{\mathbf{W}}\bar{\Lambda}\bar{\mathbf{W}}^T = \bar{\mathbf{Y}}\bar{\mathbf{Y}}^T = F\bar{\mathbf{X}}\bar{\mathbf{X}}^T F^T = \mathbf{V}D\bar{\mathcal{I}}D^T \mathbf{V}^T. \quad (2.11)$$

This means that we have found two singular value decompositions of $\bar{\mathbf{Y}}\bar{\mathbf{Y}}^T$. We know that the matrices on the left and right have the same eigenspaces. This means, in particular, that if an eigenvalue has multiplicity one, then the according eigenspaces of \mathbf{V} and $\bar{\mathbf{W}}$ match, and the the representing eigenvectors of the eigenspace are identical up to sign. This proves the second item. For eigenvalues of multiplicity higher than one, the corresponding columns of \mathbf{V} are rotations and mirrors of $\bar{\mathbf{W}}$, which proves the first item. \square

Remark 2.7 Theorem 2.6 tells us

- (i) that orthonormalization of the training images is the basis of stable decoding. Problematic is, however, that orthonormalization may not provide us with an ordering of the singular vectors. For instance, there is no guarantee that singular vectors can be recovered according to low indices, which usually carry most of the information.
- (ii) Orthonormalization is unstable. Thus, N must be chosen small to guarantee numerical stability.

Last, we also verify that PCA can be approximately rewritten as a network, analogously as the Gram-Schmidt algorithm in Figure 3. We note that the QR decomposition is used to compute the PCA.

2.3. PCA expressed as a deep network. This subsection shows that spectral value decomposition can be expressed as a customized deep network. Thereby, we make use of the fact that **singular value decomposition (SVD)** applied to the covariance matrix $A = \mathbf{Y}\mathbf{Y}^T \in \mathbb{R}^{\bar{m} \times \bar{m}}$ from Equation 2.5 gives the principal components. In other words it is a realization of the PCA. The SVD can be implemented by iterative application of the QR -algorithm, which is the famous **Francis algorithm** [14] (see also [30, 15]). Now, we show that the QR can be approximated by a deep linear algebra network, and in turn approximating the QR decomposition in the Francis algorithms with linear algebra networks, gives a “**deep-deep**” linear algebra network realizing the PCA.

Let us denote the column vectors of A by \mathbf{a}_i , $i = 1, \dots, \bar{m}$ and denote the orthonormalized vectors by $\bar{\mathbf{a}}_i$, $i = 1, \dots, \bar{m}$. Moreover, let

$$\rho(\mathbf{a}_j) := \mathbf{a}_j - \sum_{i=1}^{j-1} \langle \mathbf{a}_j, \bar{\mathbf{a}}_i \rangle \bar{\mathbf{a}}_i.$$

Then it follows (see [27], which is the elementary exposition where the formulas are used precisely in the same way as they are used here):

$$\mathbf{a}_j = \|\rho(\mathbf{a}_j)\| \bar{\mathbf{a}}_j + \sum_{i=1}^{j-1} \langle \mathbf{a}_j, \bar{\mathbf{a}}_i \rangle \bar{\mathbf{a}}_i, \quad j = 1, \dots, \bar{m}. \quad (2.12)$$

Writing this in matrix notation reads as follows:

$$A = QR \text{ with } Q = (\bar{\mathbf{a}}_1, \dots, \bar{\mathbf{a}}_n) \text{ and } R_{i,j} = \begin{cases} \langle \mathbf{a}_j, \bar{\mathbf{a}}_i \rangle & \text{for } i = 1, \dots, j-1 \\ \|\rho(\mathbf{a}_j)\| & \text{for } i = j \\ 0 & \text{for } i = j+1, \dots, \bar{m} \end{cases}. \quad (2.13)$$

In fact, it follows from Equation 2.12:

$$\bar{\mathbf{a}}_j = \frac{1}{\|\rho(\mathbf{a}_j)\|} \left(\mathbf{a}_j - \sum_{i=1}^{j-1} \langle \mathbf{a}_j, \bar{\mathbf{a}}_i \rangle \bar{\mathbf{a}}_i \right) = \sigma(\rho(\mathbf{a}_j)), \quad j = 1, \dots, \bar{m}, \quad (2.14)$$

Figure 3 with \mathbf{x} replaced by \mathbf{a} is the net, which determines Q . This shows that the matrix Q from the QR -algorithm can be determined with a **linear algebra network**. Moreover, it has been recently observed that matrix multiplication can be implemented very efficiently via reinforcement learning or, in other words, via nets (see [13]). The demystification is that tensor products are prime examples of fully connected networks. We mention that already Wilkinson [29, Sect. 35] stated that writing QR as Gram-Schmidt orthonormalization might lead to unstable implementations. Thus, the exposition above is only used for theoretical purposes.

Remark 2.8 In the last years PCA-networks have become popular in the machine learning community (see [5, 28, 24]). The goal there is somehow different and consists in minimizing the parameters of a network. Such networks could indeed be useful to investigate here on top, but this is beyond the scope of this paper.

3. IMAGE REPRESENTATION AND DECODER

We consider the decoder as represented in Figure 2. We calculate the least-squares approximation of \mathbf{y} with respect to the basis $\{\psi_l : l = 1, \dots, N\}$ (see Theorem 2.6) of eigenvectors of A . This is given by

$$\mathbf{y}_{ls} = \sum_{l=1}^N \langle \mathbf{y}, \psi_l \rangle \psi_l. \quad (3.1)$$

The goal is to find an explicit representation of the **decoding function** \mathbf{x}_{ls} . That is a function with minimal norm, which satisfies

$$F\mathbf{x}_{ls} = \mathbf{y}_{ls} \quad (3.2)$$

and which can be represented by the training pairs alone.

From [Theorem 2.6](#) it follows that for every ψ_l there exists $k(l) \in \mathbb{N}$ such that

$$\psi_l \in E^{k(l)}.$$

We denote the dimension of $E^{k(l)}$ with $m(l)$. Or, in other words, the multiplicity of γ_l is $m(l)$. From [Equation 2.8](#) we know that

$$\psi_l \in \text{span} \left\{ \mathbf{v}^{l(j)} : j = 1, \dots, m(l) \right\} = E^{k(l)}.$$

In other words

$$\psi_l = \sum_{j=1}^{m(l)} \nu_j \mathbf{v}^{l(j)}. \quad (3.3)$$

Applying [Equation 2.5](#) and [Equation 2.8](#) then implies that

$$\psi_l = \sum_{j=1}^{m(l)} \nu_j \mathbf{v}^{l(j)} = \frac{1}{\hat{\gamma}^{k(l)}} F \left(\sum_{j=1}^{m(l)} \nu_j \mathbf{u}^{l(j)} \right).$$

We summarize the calculations now in the following lemma:

Lemma 3.1 (Decoder) *The minimum norm solution of [Equation 3.2](#) is given by*

$$x_{ls} = \sum_{l=1}^N \langle \mathbf{y}, \psi_l \rangle \left(\frac{1}{\hat{\gamma}^{k(l)}} \sum_{j=1}^{m(l)} \nu_j \mathbf{u}^{l(j)} \right) = \sum_{l=1}^N \frac{\langle \mathbf{y}, \psi_l \rangle}{(\hat{\gamma}^{k(l)})^2} F^* \left(\sum_{j=1}^{m(l)} \nu_j \mathbf{v}^{l(j)} \right) = \sum_{l=1}^N \frac{\langle \mathbf{y}, \psi_l \rangle}{(\hat{\gamma}^{k(l)})^2} F^* \psi_l, \quad (3.4)$$

and therefore is a decoder.

Remark 3.2 [Lemma 3.1](#) is implemented as follows. QR decomposition is implemented to get the eigenfunction (ψ_l) , from which a decoder is implemented via [Equation 3.4](#).

4. NUMERICAL SIMULATIONS

We consider two simulation scenarios: First we prove that the singular value decomposition from training pairs is feasible. Secondly, we study a reconstruction test with a learned operator. In both cases, we use the Radon transform for two-dimensional images as the physical model for the forward operator, leveraging its analytically known singular value decomposition. (see [\[9, 22\]](#)).

4.1. SVD from training pairs. We verify numerically that orthonormalization of data $(\mathbf{x}_i \rightarrow \bar{\mathbf{x}}_i, i = 1, \dots, N)$ and a principal component analysis of $\{\bar{\mathbf{y}}_i = F(\bar{\mathbf{x}}_i) : i = 1, \dots, N\}$ (see [Equation 2.3](#) and [Equation 2.4](#)) provides us with the singular value decomposition of the discrete operator F (see [Figure 2](#)).

We take as a prototype example for F the Radon transform in two dimensions (see [Definition 4.2](#) below). The singular value decomposition of the Radon transform has been computed in [\[9\]](#) (see also [\[22\]](#)) for the general case of images of n variables. In particular for $n = 2$ we consider the Radon transform as an operator from $L^2(\mathcal{B}(0, 1))$ into $L^2(Z, w^{-1})$, where $\mathcal{B}(0, 1)$ is the unit disk in \mathbb{R}^2 centered at the origin, $Z = \mathbb{S}^1 \times [-1, 1]$, and $w(s) = (1 - s^2)^{1/2}$ is a weight function. This means that $L^2(Z, w^{-1})$ is the weighted L^2 -space with norm

$$\|g\|_{L^2(Z, w^{-1})} = \int_{\mathbb{S}^1} \int_{-1}^1 |g(\omega, s)|^2 w(s)^{-1} ds d\omega.$$

for $g \in L^2(Z, w^{-1})$. Before diving into the numerical details, we provide the necessary notational clarifications and preliminary information to facilitate the analysis.

Convention 4.1 For $\vec{\omega} = (\omega_1, \omega_2)^T \in \mathbb{S}^1$ we use the angular representation $\phi = \tan^{-1}(\omega_2/\omega_1) \in [0, 2\pi)$, which therefore satisfies

$$\omega_1 = \cos(\phi) \text{ and } \omega_2 = \sin(\phi). \quad (4.1)$$

Moreover, the orthogonal vector related to $\vec{\omega}$ is given by $\vec{\omega}^\perp = (-\sin(\phi), \cos(\phi))^T$.

For the reader's convenience we recall the definition of the Radon transform for functions on the unit disk in \mathbb{R}^2 :

Definition 4.2 (Radon transform on the unit disk) Let $Z := \mathbb{S}^1 \times [-1, 1]$. We define the Radon transform as

$$R : L^2(\mathcal{B}(0, 1)) \rightarrow L^2(Z, w^{-1}).$$

$$f \mapsto R[f](\vec{\omega}, s) = \int_{-\sqrt{1-s^2}}^{\sqrt{1-s^2}} f(s\vec{\omega} + t\vec{\omega}^\perp) dt \quad (4.2)$$

One can show that this operator is continuous and satisfies (see [9]):

$$\|R[f]\|_{L^2(Z, w^{-1})} \leq \sqrt{4\pi} \|f\|_{L^2(\mathcal{B}(0, 1))}.$$

In the following, we recall the expression of the adjoint operator of the Radon-transform R defined on the unit disk. This is the operator $R^* : L^2(Z, w^{-1}) \rightarrow L^2(\mathcal{B}(0, 1))$, which satisfies

$$\langle R[f], g \rangle_{L^2(Z, w^{-1})} = \langle f, R^*[g] \rangle_{L^2(\mathcal{B}(0, 1))}.$$

Definition 4.3 (Adjoint) For every $g \in L^2(Z, w^{-1})$ and almost all $\vec{x} = (x_1, x_2)^T \in \mathbb{R}^2$ the adjoint of the Radon-transform R^* is given by

$$R^*[g](\vec{x}) = \int_{\mathbb{S}^1} \frac{g(\vec{\omega}, \vec{x} \cdot \vec{\omega})}{w(\vec{x} \cdot \vec{\omega})} d\vec{\omega}.$$

In the following we give a survey on the singular value decomposition (SVD) of the Radon transform for functions on the unit disk. The results are essentially taken from [22] with the main difference that we consider the adjoint R^* restricted to the range of R (in contrast to Definition 4.3).

Before recalling the spectral decomposition of the Radon-transform, we review the general definition of a spectral decomposition:

Definition 4.4 (Spectral decomposition, [12]) Let $K : X \rightarrow Y$ be a compact linear operator. A **singular system** $(u_k, v_k; \gamma_k)$ is defined as follows:

- (i) $\gamma_k^2, k \in \mathbb{N}_0$ are the non-zero eigenvalues of the selfadjoint operator K^*K (and also KK^*) written in decreasing order. We always take $\gamma_k > 0$.
- (ii) $\frac{u_k}{\gamma_k}, k \in \mathbb{N}_0$ are a complete orthonormal system of eigenvectors of K^*K (on the space $\overline{\mathcal{R}(K^*)} = \overline{\mathcal{R}(K^*K)}$).
- (iii) $v_k := \frac{1}{\|Ku_k\|} Ku_k, k \in \mathbb{N}_0$.

The set $\{v_k : k \in \mathbb{N}_0\}$ are a complete orthonormal system of eigenvectors of KK^* which span $\overline{\mathcal{R}(K)} = \overline{\mathcal{R}(KK^*)}$. Moreover, the following formulas hold:

$$Ku_k = \gamma_k v_k, \quad K^*u_k = \gamma_k v_k,$$

$$Kx = \sum_{k=0}^{\infty} \gamma_k \langle x, u_k \rangle v_k \text{ for all } x \in X, \quad K^*y = \sum_{k=0}^{\infty} \gamma_k \langle y, v_k \rangle u_k \text{ for all } y \in Y.$$

Theorem 4.5 [22, p 99] *The spectral decomposition of the Radon transform is given by $\{(u_{k,l}, v_{k,l}; \gamma_{k,l}) : (k, l) \in \mathcal{I}\}$ where*

- (i) $\mathcal{I} = \{(k, l) : k \in \mathbb{N}_0, l \in \{0, 1, \dots, k\}, \text{ satisfying } l + k \text{ is even}\}$.
- (ii) $\gamma_k^2 = \gamma_{k,l}^2 = \frac{4\pi}{k+1} > 0$ is independent of l .

(iii) Let Y_s be the spherical harmonics in \mathbb{R}^2 and let

$$s \mapsto C_k(s) = \frac{\sin((k+1) \arccos(s))}{\sin(\arccos(s))}$$

denote the Chebyshev polynomials of the second kind. Moreover, let

$$\frac{1}{c(k)} = \|wC_k Y_{k-2l}\|_{L^2(Z, w^{-1})} = \|\sqrt{w}C_k\|_{L^2(-1,1)}.$$

Then the normalized eigenfunctions of RR^* on the orthogonal complement of the nullspace of R^* , \mathcal{N}^\perp are given by

$$(s, \omega) \rightarrow v_{k,l}(s, \omega) := c(k)w(s)C_k(s)Y_{k-2l}(\omega) \text{ and } u_{k,l} = \frac{1}{\gamma_k}R^*[v_{kl}]. \quad (4.3)$$

The calculation of the singular value decomposition of the Radon transform has been computed in several work (see for instance [9, 21, 22] and [23, Theorem 6.4] to mention but a few).

Remark 4.6 (i) The existence of a singular value decomposition with $\gamma_k \rightarrow 0$ in particular shows that the Radon-transform is compact.

(ii) From Theorem 4.5, item (i) and item (ii) we see that, in general, γ_k has multiplicity higher than one. The sets E^k associated to a spectral value γ_k are spanned by the spectral functions v_{kl} with l such that $(k, l) \in \mathcal{I}$. For example, taking $k = 0, \dots, 7$, and $l = 0, \dots, k$, with $k + l$ even (meaning that $(k, l) \in \mathcal{I}$), we have

$$\begin{aligned} E^1 &= \text{span}\{v_{0,0}\}, & E^2 &= \text{span}\{v_{1,1}\}, & E^3 &= \text{span}\{v_{2,0}, v_{2,2}\}, & E^4 &= \text{span}\{v_{3,1}, v_{3,3}\}, \\ E^5 &= \text{span}\{v_{4,0}, v_{4,2}, v_{4,4}\}, & E^6 &= \text{span}\{v_{5,1}, v_{5,3}, v_{5,5}\}, & E^7 &= \text{span}\{v_{6,0}, v_{6,2}, v_{6,4}, v_{6,6}\}, \\ E^8 &= \text{span}\{v_{7,1}, v_{7,3}, v_{7,5}, v_{7,7}\}. \end{aligned} \quad (4.4)$$

It is an interesting fact stated in [22] that the adjoint of the Radon-transform R^* has a nullspace. In fact the nullspace of R^* is given by

$$\mathcal{N} = \{v_{k,l} : k \in \mathbb{N}_0, l \in \{0, 1, \dots, k\}, \text{ satisfying } l + k \text{ is odd}\}.$$

In fact also RR^* has the same nullspace, which is shown for instance in [22, p. 99].

4.2. Numerical simulations. In this section, we present two numerical experiments:

- (i) The first tests concern computing the SVD of the Radon-transform in two test scenarios:
 - (a) **Learning spectral functions from analytical spectral functions:** We use as training data $(\mathbf{x}_i, \mathbf{y}_i)$, $i = 1, \dots, 49$ the first 49, analytical given, spectral functions (u_{kl}, v_{kl}) , defined in Equation 4.3. We compare the outcome with our orthonormalization approach.
 - (b) **Learning spectral functions from arbitrary test functions:** Here we use annotations of images, which are orthonormalized. This is of course a much harder problem.
- (ii) We are concerned with decoding by making use of Equation 3.4. Here we use both singular value decompositions obtained in the first step.

4.2.1 Singular value decomposition

We visualize the first twenty benchmark images, which are the singular functions $u_{k,l}, v_{k,l}$ with $(l, k) \in \mathcal{I}$ of the Radon-transform outlined in Theorem 4.5, Figure 4 and Figure 5. These plots are used to visualize the difference between some of the benchmark data and the learned singular functions. We emphasize that in the learned approaches we reconstruct vectors $u_{k,l} \in \mathbb{R}^m$ and $v_{k,l} \in \mathbb{R}^{\bar{m}}$, with $m = \bar{m} = 2500$. However, we maintain the same notation used in the theoretical part. We note that the first 49 non-zero eigenvalues of RR^* belong to the following 12 distinct singular values

$$\Gamma = \{\gamma_{0,0}, \gamma_{1,1}, \gamma_{2,0}, \gamma_{3,1}, \gamma_{4,0}, \gamma_{5,1}, \gamma_{6,0}, \gamma_{7,1}, \gamma_{8,0}, \gamma_{9,1}, \gamma_{10,0}, \gamma_{11,1}, \gamma_{12,0}\}. \quad (4.5)$$

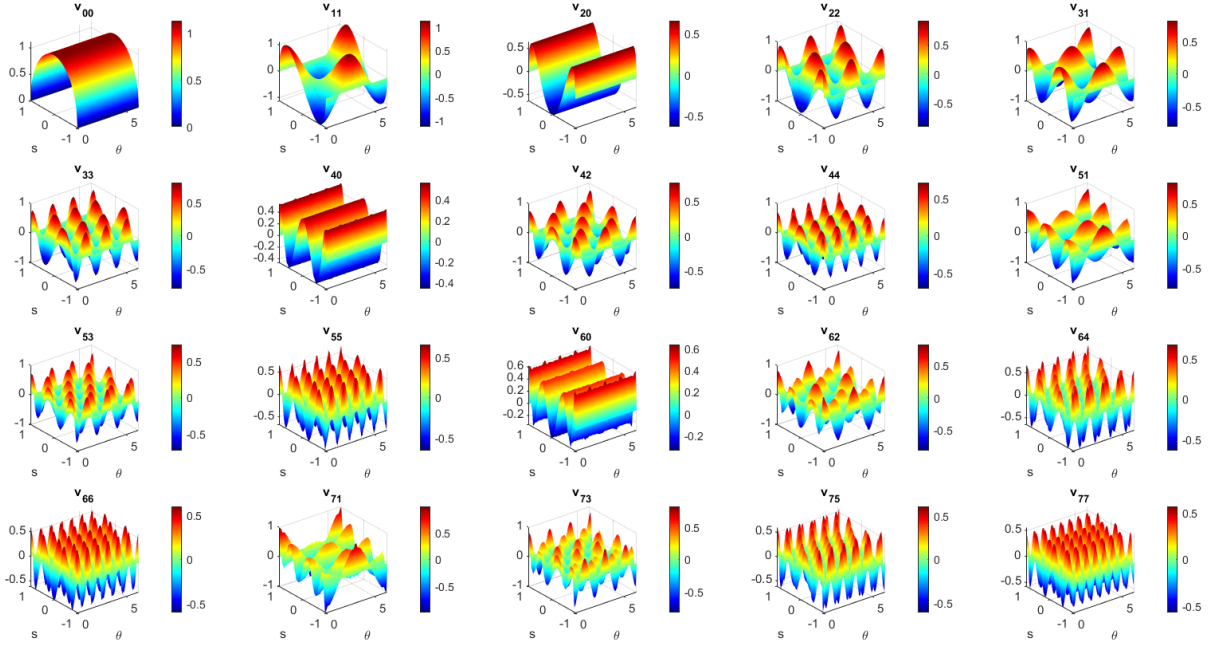


FIGURE 4. This plot visualizes the first twenty normalized singular functions v_{kl} , defined in Equation 4.3, for $k = 0, 1, \dots, 7$, $l = 0, 1, \dots, k$ and $l + k$ even.

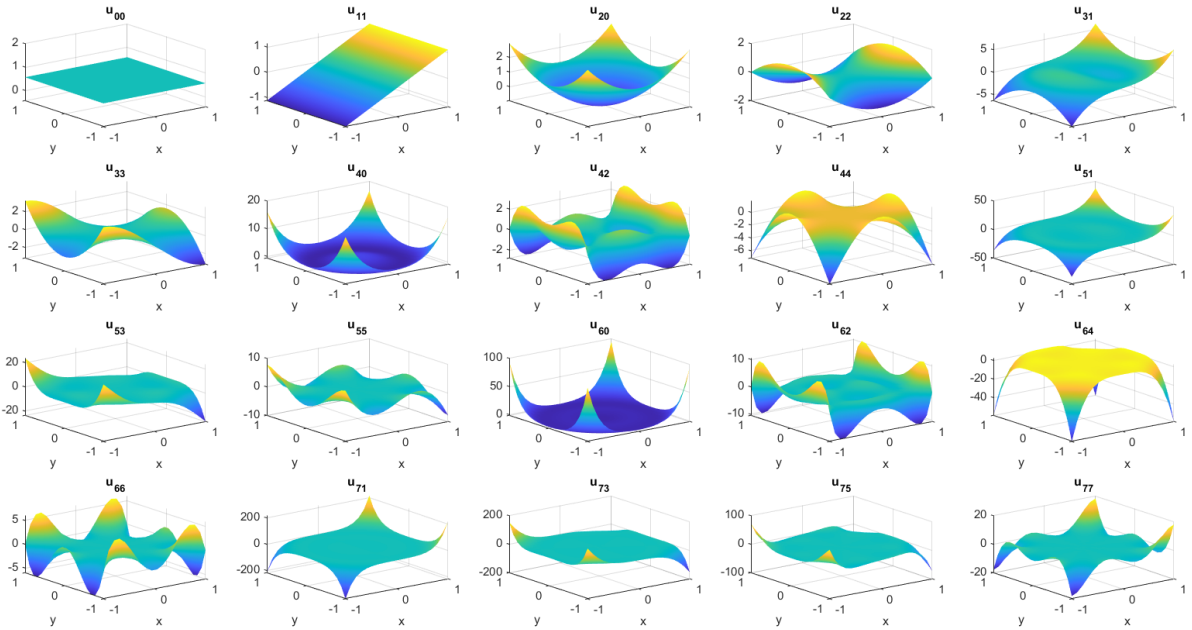


FIGURE 5. This plot visualizes the first twenty singular functions u_{kl} , defined in Equation 4.3, for $k = 0, 1, \dots, 7$, $l = 0, 1, \dots, k$ and $l + k$ even.

Example 4.7 (Learning spectral functions from analytical spectral functions) We start with a basic test by learning the spectral functions of the Radon-transform from input of the column vectors $\bar{y}_{k,l} := v_{k,l}$, which are discretizations of the spectral functions of the Radon-transform as written down in Equation 4.3. This should be the most simple test-case and the results should return discrete singular functions of the analytical singular functions. To be specific, we want to verify Theorem 2.6 numerically. For this purpose, we construct the matrix \bar{Y} consisting of the first 49 singular functions (column vectors) $\bar{y}_{k,l} = v_{k,l}$ (some of them are shown in Figure 4) and the according matrix $A = \bar{Y}\bar{Y}^T \in \mathbb{R}^{\bar{m} \times \bar{m}}$ and $\bar{Y} \in \mathbb{R}^{\bar{m} \times 49}$, with $\bar{m} = 2500$. In Figure 6, we show the first twenty results obtained from the singular value decomposition of A , graphically representing the eigenvectors of the matrix $\bar{W} = (\psi_1, \dots, \psi_{49})$ as

defined in Equation 2.10 in Theorem 2.6.

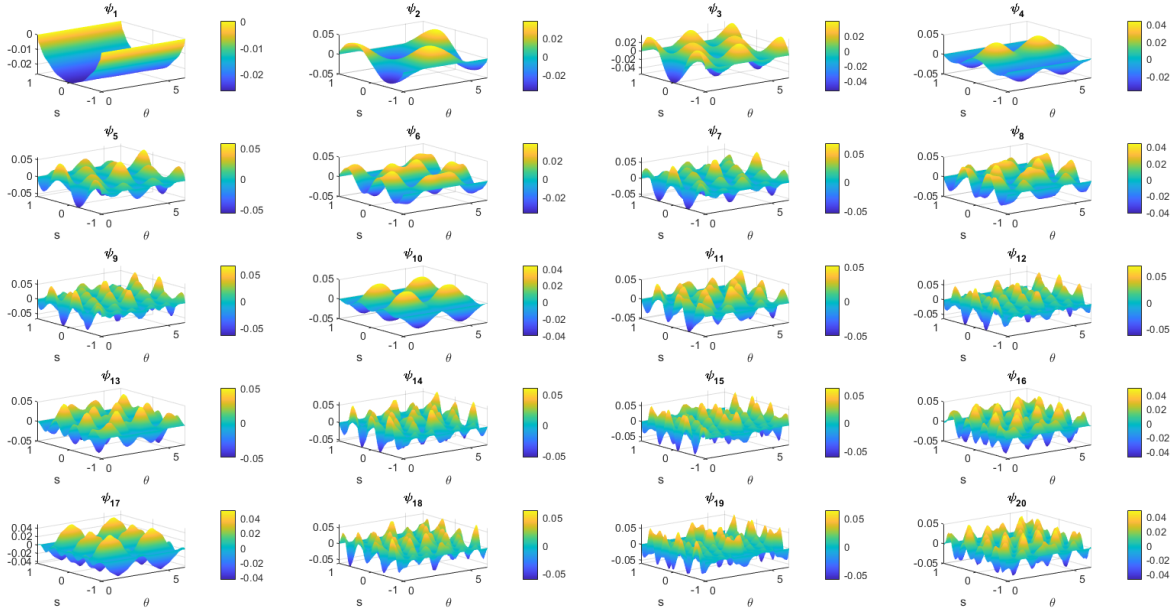


FIGURE 6. This plot shows the first twenty functions ψ_h obtained from the singular value decomposition of the matrix A , defined in Equation 2.9 with column vectors $\bar{y}_{kl} := v_{kl}$. These results should be compared with $v_{k,l}$ as plotted in Figure 4. It is obvious that if a singular value has multiplicity 1, then $v_{0,0}$ is also an eigenfunction, so ψ_1 perfectly represents the claim. For higher indices linear combinations are reconstructed approximately.

Example 4.8 Comparing the results from analytical and learned singular value decomposition reveals what has been stated in Theorem 2.6 that in case of eigenvalues of RR^* with multiplicity higher than one only the according eigenspace can be reconstructed. In other words every ψ_h should be able to be written as a linear combination of the according functions v_{kl} with $(k, l) \in \mathcal{I}$ with some index l , which needs to be identified in addition.

Using the eigenspaces E^k , for $k = 1, \dots, 13$, according to the spectral value γ_k , as defined in Theorem 2.6, we identify the sets to which the numerically calculated functions ψ_h , for $h = 1, \dots, 49$ most likely belong. This is a two-step process as discussed below:

- (i) Identifying the set E^k , which ψ_h most likely belongs to: We obtained with our Matlab code the classification given in Table 1
- (ii) Finding an appropriate linear combination of basis-elements of E^k , which optimally approximates ψ_h , for $h = 1, \dots, 49$. For example, applying MATLAB's linear regression techniques, we obtained the following visual results, see Figure 7, for the functions ψ_h , where $h = 1, 2, 3, 4, 38, 49$. Each plot displays: (1) the original function ψ_h to be approximated, (2) the approximation using the best set of functions E^k (see Table 1), and (3) the approximation error. For example, regarding the coefficients of the linear combinations for the functions ψ_h , where $h = 1, 2, 3, 4, 38, 49$, we have the results in Table 2.

The numerical reconstructions of the singular functions is satisfying for the first twelve (the first four are shown in the first and second line of Figure 7). After that the errors are pronounced, with values of the same order of magnitude as those of the functions ψ_h (see, for example, the plots of the last line in Figure 7).

The example has shown that reconstruction of the singular functions and values of operators is possible from training data without knowing the operator explicitly. But the higher oscillating the functions are the more complicated it gets numerically.

Example 4.9 (Learning spectral functions from arbitrary test functions) In this example, we consider a dataset, composed of twenty elements, that we have constructed by ourself using a Matlab

Set	Singular Values
E^1	ψ_1
E^2	ψ_2
E^3	ψ_3, ψ_4
E^4	ψ_5, ψ_6
E^5	ψ_7
E^6	ψ_9
E^7	ψ_8, ψ_{10}
E^8	ψ_{11}, ψ_{13}
E^9	$\psi_{12}, \psi_{14}, \psi_{16}, \psi_{17}$
E^{10}	$\psi_{15}, \psi_{18}, \psi_{20}, \psi_{22}, \psi_{23}, \psi_{45}, \psi_{46}$
E^{11}	$\psi_{19}, \psi_{21}, \psi_{24}, \psi_{25}, \psi_{26}, \psi_{27}, \psi_{44}, \psi_{47}, \psi_{48}, \psi_{49}$
E^{12}	$\psi_{28}, \psi_{30}, \psi_{31}, \psi_{33}, \psi_{34}, \psi_{39}, \psi_{41}, \psi_{43}$
E^{13}	$\psi_{29}, \psi_{32}, \psi_{35}, \psi_{36}, \psi_{37}, \psi_{38}, \psi_{40}, \psi_{42}$

TABLE 1. Set E^k which ψ_h most likely belongs to.

Set	Linear Combination
E^1	$\psi_1 = -0.02188v_{0,0}$
E^2	$\psi_2 = 0.03360v_{1,1}$
E^3	$\psi_3 = 0.01243v_{2,0} + 0.03831v_{2,2}, \psi_4 = -0.03693v_{2,0} + 0.01436v_{2,2}$
E^{11}	$\psi_{49} = 0.02541v_{10,0} - 0.01122v_{10,2} - 0.00060v_{10,4} - 0.00072v_{10,6} - 0.00061v_{10,8} + 0.00003v_{10,10}$
E^{13}	$\psi_{38} = 0.04555v_{12,0} - 0.02561v_{12,2} - 0.00396v_{12,4} - 0.00004v_{12,6} + 0.00012v_{12,8} + 0.00003v_{12,10} - 0.00153v_{12,12}$

TABLE 2. ψ_h , for $h = 1, 2, 3, 4, 38, 49$, as linear combinations of the eigenfunctions v_{kl} .

function. Specifically, each discrete image, of numerical dimension 50×50 , is composed of ten ellipses that have been generated randomly. In fact, we want to create several images that mimic the structure of the Shepp-Logan phantom. Each ellipse is described by assigning seven parameters (intensity, length of the major semi-axis, length of the minor semi-axis, x-coordinate of the center, y-coordinate of the center, rotation angle) that vary within the ranges reported in the Table 3. In Figure 8 and Figure 9,

Parameter of Ellipse	Range
Intensity	[0.01, 2]
Length of the major semi-axis	[0.1, 0.7]
Length of the minor semi-axis	[0.1, 0.7]
x-coordinate of the center	[-0.6, 0.6]
y-coordinate of the center	[-0.6, 0.6]
Rotation angle	[-45°, 134°]

TABLE 3. Parameters and their corresponding ranges for the ellipses of the dataset described in Example 4.9.

we present the plot of the images constructed with our MATLAB routine and their orthonormalized version (in Figure 9, we show the projection of the values onto the xy plane for better visualization of the orthonormalization procedure). The corresponding data (that is the sinograms) of the orthonormalized

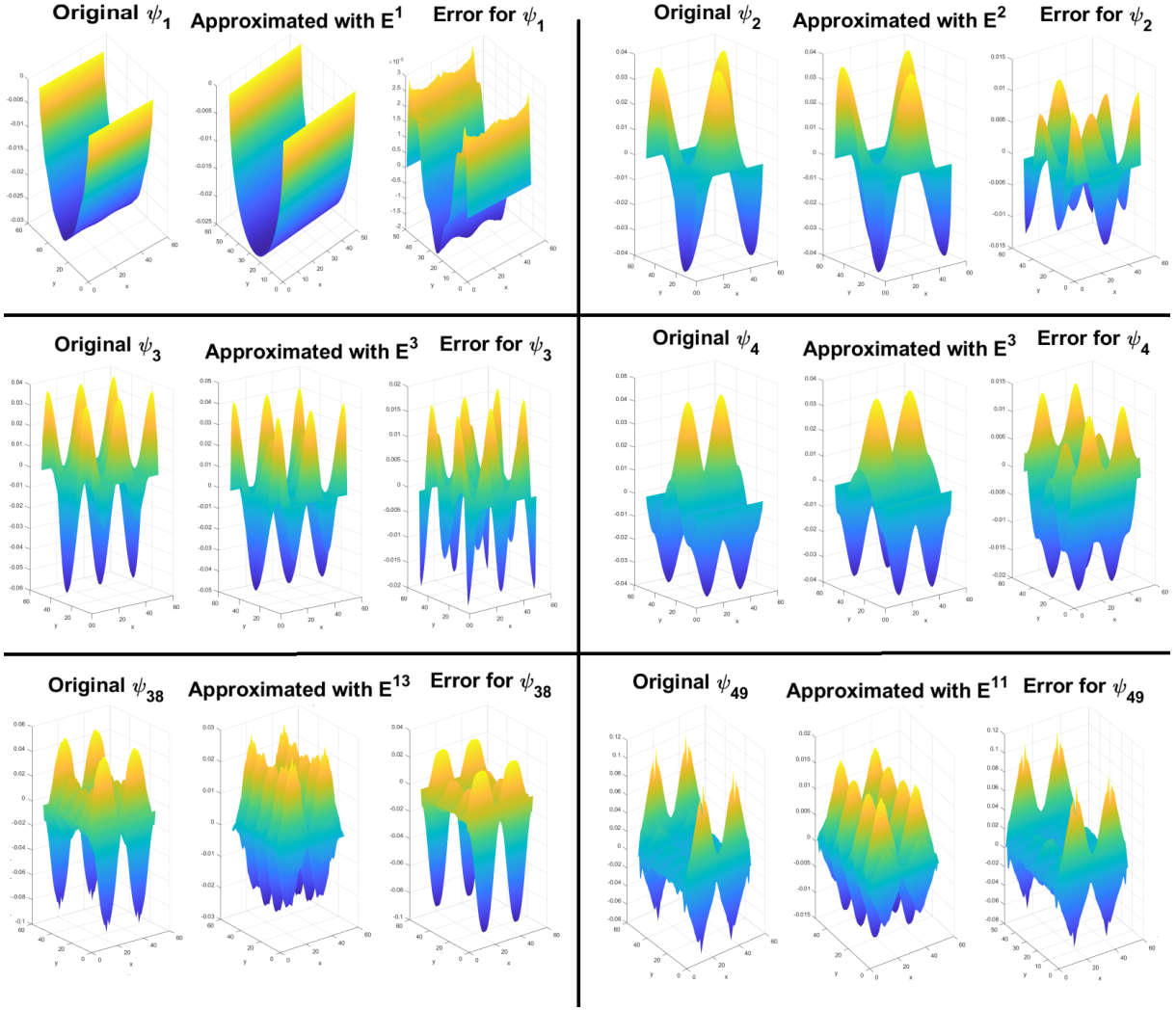


FIGURE 7. Results of the linear combinations for ψ_h , with $h = 1, 2, 3, 4, 38, 49$.

images, see Equation 2.3, $\bar{y}_k = R(\bar{x}_k)$ are plotted in Figure 10. As in the previous numerical example, see Example 4.7, we utilize the eigenspaces E^k for $k = 1, \dots, 8$, to identify the sets to which the numerically computed functions ψ_h , for $h = 1, \dots, 20$ most likely belong. We obtained with our Matlab code the classification given in Table 4. As before, we identify suitable linear combinations of elements of E^k in order to rewrite the term ψ_h . We present in Figure 11 the first four results of the linear combinations, allowing for a direct comparison with the outcomes previously obtained in Example 4.7. The reader can observe, as expected, that the approximation results, expressed as linear combinations, are less precise than those found in Example 4.7.

4.2.2 Decoding

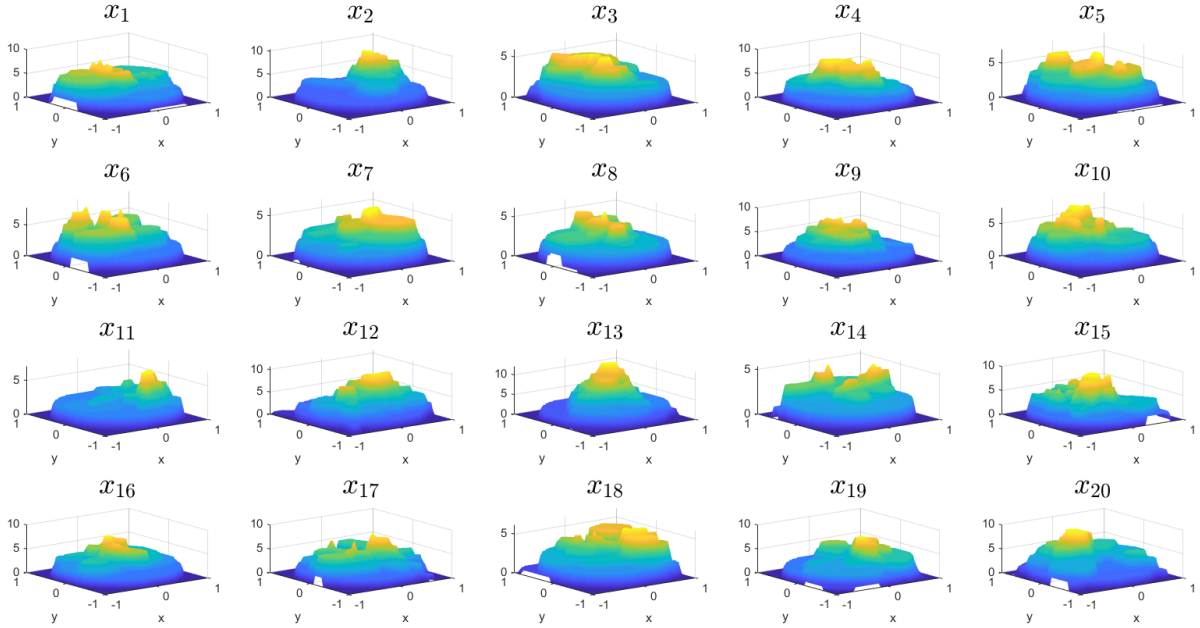
Using the results from the previous subsection, we implement the reconstruction formula derived in Equation 3.4.

Test 1: In the first example the ground truth is given by

$$\begin{aligned} \mathbf{x}_{true} = & -0.9119\mathbf{u}_{11,5} + 0.6527\mathbf{u}_{3,1} - 0.7343\mathbf{u}_{6,4} + 0.5406\mathbf{u}_{5,3} \\ & + 0.9758\mathbf{u}_{8,4} - 0.1569\mathbf{u}_{12,10} + 0.2778\mathbf{u}_{7,3} + 0.6395\mathbf{u}_{12,2}. \end{aligned} \quad (4.6)$$

In Figure 12 the numerical reconstruction with the decoder Equation 3.4 is plotted. It provides a reasonable reconstruction.

Test 2. We introduce a scenario similar to **Test 1**, but now involving a nonlinear combination of functions $\mathbf{u}_{k,l}$. Specifically, for each function $\mathbf{u}_{k,l}$ in the nonlinear combination, we apply the

FIGURE 8. Images x_k , for $k = 1, \dots, 20$.

Set	Singular Values
E^1	ψ_1
E^2	ψ_2, ψ_3
E^3	ψ_4, ψ_5, ψ_6
E^4	ψ_9
E^5	ψ_{10}
E^6	$\psi_7, \psi_8, \psi_{18}, \psi_{19}$
E^7	$\psi_{11}, \psi_{12}, \psi_{13}, \psi_{14}, \psi_{17}, \psi_{20}$
E^8	ψ_{15}, ψ_{16}

TABLE 4. Set E^k which ψ_h most likely belongs to in the case of [Example 4.9](#).

operation $0.1\mathbf{u}_{k,l}^2 + e^{\mathbf{u}_{k,l}/\max(\mathbf{u}_{k,l})}$, scaled by a specific weight. Results and comparison with ground truth are provided in [Figure 13](#). As expected, in the nonlinear setting the results are worse.

CONCLUSION

In this paper we have shown that a double orthonormalization strategy, consisting first of orthonormalization of training images and second of a principal component analysis of the training data theoretically provides us with the singular value decomposition of a linear operator (without making use of an explicit physical model). Two further interesting aspects are shown: First: Orthonormalization, like Gram-Schmidt, can be expressed as a deep neural network, and this opens up exploiting synergies with de- and encoder strategies. Secondly, not only the singular value decomposition can be implemented purely data driven but also the decoding, meaning that for arbitrary data the minimum-norm solution can be computed data driven.

Acknowledgements. This research was funded in whole, or in part, by the Austrian Science Fund (FWF) P 34981 – New Inverse Problems of Super-Resolved Microscopy (NIPSUM). For the purpose of

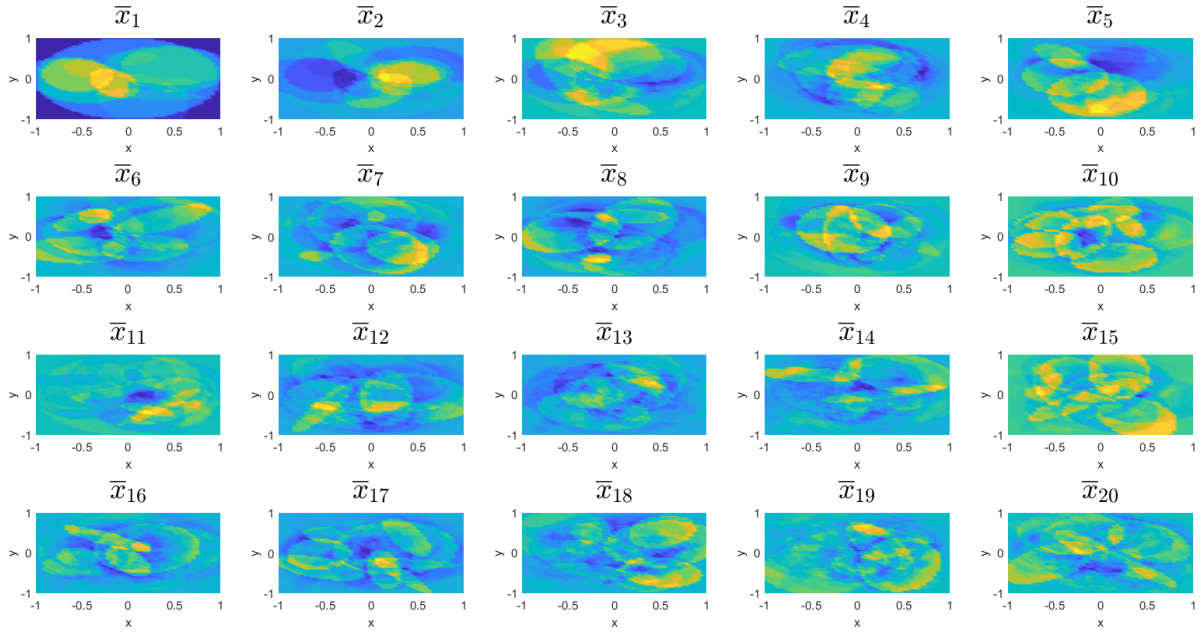


FIGURE 9. Orthonormalized images \bar{x}_k , for $k = 1, \dots, 20$, projected onto the plane xy .

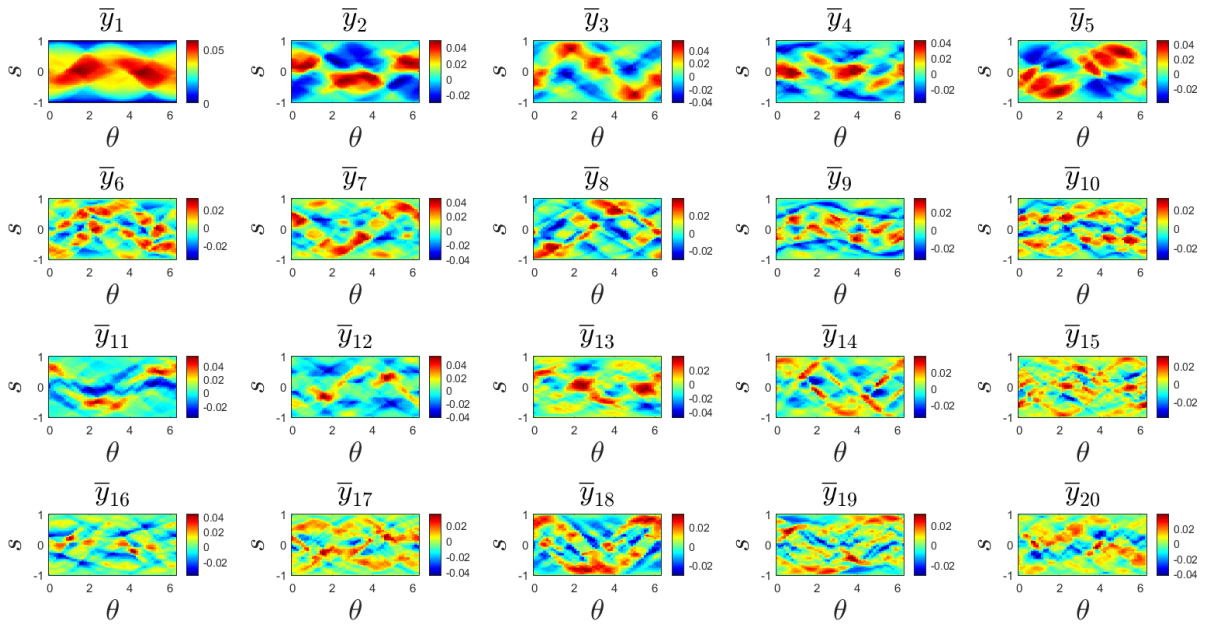


FIGURE 10. Data \bar{y}_k , for $k = 1, \dots, 20$.

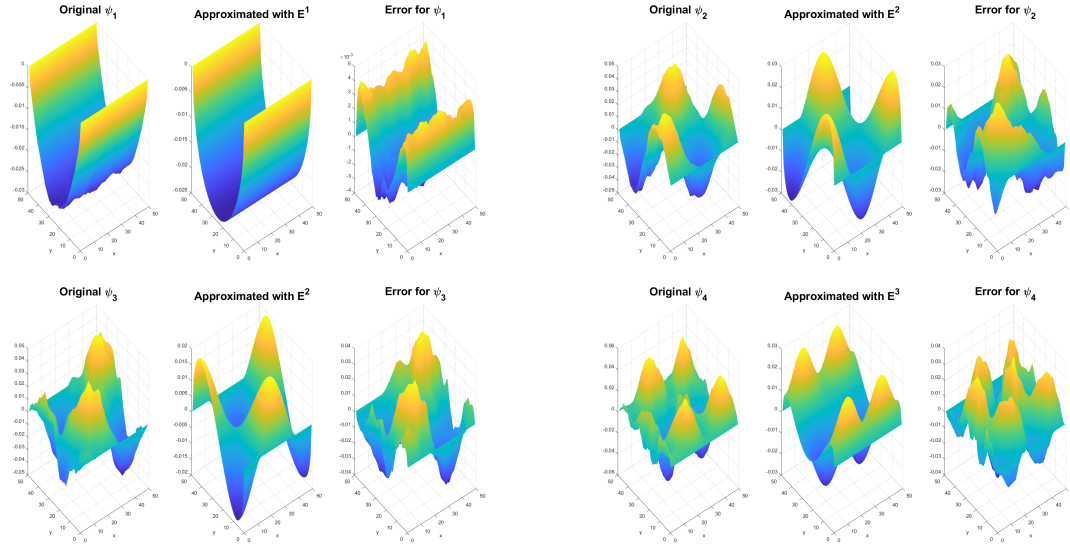


FIGURE 11. Results of the linear combinations for ψ_h , with $h = 1, 2, 3, 4$.

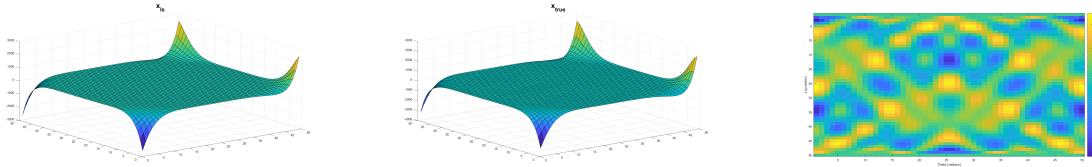


FIGURE 12. Decoding, ground truth as represented in Equation 4.6 and y_{true} .

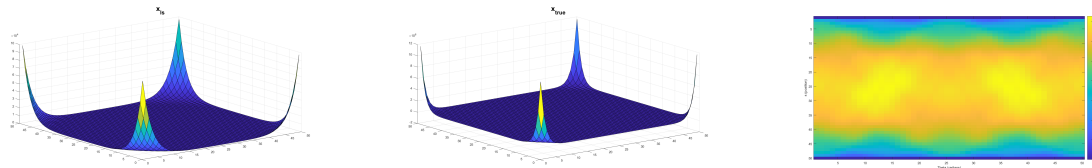


FIGURE 13. Decoding, ground truth as represented in Equation 4.6 and y_{true} in the nonlinear combination setting.

open access, the author has applied a CC BY public copyright license to any Author Accepted Manuscript version arising from this submission. Moreover, OS is supported by the Austrian Science Fund (FWF), with SFB F68 “Tomography Across the Scales”, project F6807-N36 (Tomography with Uncertainties). The financial support by the Austrian Federal Ministry for Digital and Economic Affairs, the National Foundation for Research, Technology and Development and the Christian Doppler Research Association is gratefully acknowledged. AA is member of the group GNAMPA (Gruppo Nazionale per l’Analisi Matematica, la Probabilità e le loro Applicazioni) of INdAM (Istituto Nazionale di Alta Matematica). The computational results presented have been achieved in part using the Vienna Scientific Cluster (VSC). The authors want to thank Martin Rumpf (University of Bonn) for stimulating discussions and feedback.

REFERENCES

- [1] S. Arridge, P. Maass, O. Öktem, and C.-B. Schönlieb. “Solving inverse problems using data-driven models”. In: *Acta Numerica* 28 (2019), pp. 1–174. ISSN: 0962-4929. DOI: [10.1017/s0962492919000059](https://doi.org/10.1017/s0962492919000059) (cited on page 1).
- [2] A. Aspri. *Source code for learning linear operators solely through training pairs by applying encoding and decoding procedures, without directly utilizing the operators themselves*. 2024. <https://gitlab.com/csc1/learning-op> (commit 66893bab), <https://phaidra.univie.ac.at/o:2087334> (cited on page 2).

-
- [3] A. Aspri, L. Frischauf, Y. Korolev, and O. Scherzer. “Data Driven Reconstruction Using Frames and Riesz Bases”. In: *Deterministic and Stochastic Optimal Control and Inverse Problems*. Ed. by B. Jadamba, A. A. Khan, S. Migórski, and M. Sama. CRC Press, 2021, pp. 303–318. DOI: [10.1201/9781003050575-13](https://doi.org/10.1201/9781003050575-13) (cited on pages 1, 2).
- [4] A. Aspri, Y. Korolev, and O. Scherzer. “Data driven regularization by projection”. In: *Inverse Problems* 36.12 (Dec. 2020), p. 125009. ISSN: 0266-5611. DOI: [10.1088/1361-6420/abb61b](https://doi.org/10.1088/1361-6420/abb61b) (cited on pages 1, 2).
- [5] K. Bhattacharya, B. Hosseini, N. B. Kovachki, and A. M. Stuart. “Model Reduction and Neural Networks for Parametric PDEs”. Preprint on ArXiv 2005.03180. 2020. DOI: [10.48550/arxiv.2005.03180](https://doi.org/10.48550/arxiv.2005.03180) (cited on page 6).
- [6] C. M. Bishop. “Neural Networks for Pattern Recognition”. Oxford: Clarendon Press, 1995 (cited on page 3).
- [7] J. Braunsman, M. Rajkovic, M. Rumpf, and B. Wirth. “Learning low bending and low distortion manifold embeddings”. In: *2021 IEEE/CVF Conference on Computer Vision and Pattern Recognition Workshops (CVPRW)*. 2021. DOI: [10.1109/cvprw53098.2021.00498](https://doi.org/10.1109/cvprw53098.2021.00498) (cited on page 2).
- [8] E. Carson, K. Lund, M. Rozložník, and S. Thomas. “Block Gram-Schmidt algorithms and their stability properties”. In: *Linear Algebra and its Applications* 638 (2022), pp. 150–195. ISSN: 0024-3795. DOI: [10.1016/j.laa.2021.12.017](https://doi.org/10.1016/j.laa.2021.12.017) (cited on page 3).
- [9] M. E. Davison. “A singular value decomposition for the radon transform in n -dimensional euclidean space”. In: *Numerical Functional Analysis and Optimization* 3.3 (1981), pp. 321–340. ISSN: 0163-0563. DOI: [10.1080/01630568108816093](https://doi.org/10.1080/01630568108816093) (cited on pages 2, 7–9).
- [10] M. A. G. Duff, N. D. F. Campbell, and M. J. Ehrhardt. “Regularising Inverse Problems with Generative Machine Learning Models”. In: *Journal of Mathematical Imaging and Vision* 66.1 (2024), pp. 37–56. ISSN: 0924-9907. DOI: [10.1007/s10851-023-01162-x](https://doi.org/10.1007/s10851-023-01162-x) (cited on page 2).
- [11] J. E. van Engelen and H. H. Hoos. “A survey on semi-supervised learning”. In: *Machine Learning* 109.2 (2020), pp. 373–440. DOI: [10.1007/s10994-019-05855-6](https://doi.org/10.1007/s10994-019-05855-6) (cited on page 2).
- [12] H. W. Engl, M. Hanke, and A. Neubauer. “Regularization of inverse problems”. Mathematics and its Applications 375. Dordrecht: Kluwer Academic Publishers Group, 1996. viii+321. ISBN: 0-7923-4157-0 (cited on pages 4, 8).
- [13] A. Fawzi et al. “Discovering faster matrix multiplication algorithms with reinforcement learning”. In: *Nature* 610.7930 (2022), pp. 47–53. DOI: [10.1038/s41586-022-05172-4](https://doi.org/10.1038/s41586-022-05172-4) (cited on page 6).
- [14] J. G. F. Francis. “The QR Transformation A Unitary Analogue to the LR Transformation—Part 1”. In: *The Computer Journal* 4.3 (1961), pp. 265–271. DOI: [10.1093/comjnl/4.3.265](https://doi.org/10.1093/comjnl/4.3.265) (cited on page 6).
- [15] G. H. Golub and C. F. Van Loan. “Matrix Computations”. Baltimore: The Johns Hopkins University Press, 1996 (cited on pages 3, 4, 6).
- [16] M. Haltmeier and L. Nguyen. “Regularization of Inverse Problems by Neural Networks”. In: *Handbook of Mathematical Models and Algorithms in Computer Vision and Imaging*. 2022, pp. 1–29. DOI: [10.1007/978-3-030-03009-4_81-1](https://doi.org/10.1007/978-3-030-03009-4_81-1) (cited on page 1).
- [17] N. Kovachki, S. Lanthaler, and S. Mishra. “On Universal Approximation and Error Bounds for Fourier Neural Operators”. In: *Journal of Machine Learning Research (JMLR)* 22.290 (2021), pp. 1–76 (cited on page 1).
- [18] S. Lanthaler, Z. Li, and A. M. Stuart. “The Nonlocal Neural Operator: Universal Approximation”. Preprint on ArXiv 2304.13221. 2023. DOI: <https://doi.org/10.48550/arxiv.2304.13221> (cited on page 1).
- [19] S. Lanthaler, S. Mishra, and G. E. Karniadakis. “Error estimates for DeepONets: a deep learning framework in infinite dimensions”. In: *Transactions of Mathematics and Its Applications* 6.1 (2022). DOI: <https://doi.org/10.1093/imatrm/tnac001> (cited on page 1).
- [20] S. Lanthaler and A. M. Stuart. “The Parametric Complexity of Operator Learning”. Preprint on ArXiv 2306.15924. 2023. DOI: <https://doi.org/10.48550/arxiv.2306.15924> (cited on page 1).
- [21] P. Maass. “The X-ray transform: singular value decomposition and resolution”. In: *Inverse Problems* 3.4 (1987), pp. 729–741. ISSN: 0266-5611 (cited on page 9).

-
- [22] F. Natterer. “The Mathematics of Computerized Tomography”. Vol. 32. Classics in Applied Mathematics. Philadelphia, PA: Society for Industrial and Applied Mathematics (SIAM), 2001. xviii+222. ISBN: 0-89871-493-1. DOI: [10.1007/978-3-663-01409-6](https://doi.org/10.1007/978-3-663-01409-6) (cited on pages 2, 7–9).
- [23] F. Natterer and F. Wübbeling. “Mathematical Methods in Image Reconstruction”. Monographs on Mathematical Modeling and Computation 5. Philadelphia, PA: SIAM, 2001 (cited on page 9).
- [24] N. H. Nelsen and A. M. Stuart. “Operator Learning Using Random Features: A Tool for Scientific Computing”. In: *SIAM Review* 66.3 (2024), pp. 535–571. ISSN: 0036-1445. DOI: [10.1137/24m1648703](https://doi.org/10.1137/24m1648703) (cited on page 6).
- [25] A. Papoulis. “The Fourier Integral and its Applications”. New York: McGraw-Hill, 1962 (cited on page 1).
- [26] T. I. Seidman. “Nonconvergence results for the application of least-squares estimation to ill-posed problems”. In: *Journal of Optimization Theory and Applications* 30.4 (1980), pp. 535–547. DOI: [10.1007/bf01686719](https://doi.org/10.1007/bf01686719) (cited on page 4).
- [27] O. Steinbach. “Lösungsverfahren für lineare Gleichungssysteme”. 2005. DOI: [10.1007/978-3-322-80080-0](https://doi.org/10.1007/978-3-322-80080-0) (cited on page 6).
- [28] D. N. Tanyu, I. Michel, A. Rademacher, J. Kuhnert, and P. Maass. “Parameter identification by deep learning of a material model for granular media”. In: *GEM - International Journal on Geomathematics* 15.1 (2024). DOI: [10.1007/s13137-024-00253-0](https://doi.org/10.1007/s13137-024-00253-0) (cited on page 6).
- [29] J. H. Wilkinson. “The Algebraic Eigenvalue Problem”. Monographs on Numerical Analysis. The Clarendon Press, Oxford University Press, New York, 1988, pp. xviii+662. ISBN: 0-19-853418-3 (cited on page 6).
- [30] F. Willers. “Methoden der praktischen Analysis”. 4th ed. Berlin-New York: Walter de Gruyter, 1971 (cited on page 6).